

CHANDRA AND HUBBLE SPACE TELESCOPE STUDY OF THE GLOBULAR CLUSTER NGC 288¹

ALBERT K. H. KONG², Cees Bassa³, DAVID POOLEY^{4,7}, WALTER H. G. LEWIN², LEE HOMER⁵,
FRANK VERBUNT³, SCOTT F. ANDERSON⁵ AND BRUCE MARGON⁶

Accepted for publication in *ApJ*

ABSTRACT

We report on the *Chandra X-ray Observatory* observations of the globular cluster NGC 288. We detect four X-ray sources within the core radius and seven additional sources within the half-mass radius down to a limiting luminosity of $L_X = 7 \times 10^{30}$ ergs s⁻¹ (assuming cluster membership) in the 0.3–7 keV band. We also observed the cluster with the *Hubble Space Telescope* Advanced Camera for Surveys and identify optical counterparts to seven X-ray sources out of the nine sources within the *HST* field-of-view. Based on the X-ray and optical properties, we find 2–5 candidates of cataclysmic variables (CVs) or chromospherically active binaries, and 2–5 background galaxies inside the half-mass radius. Since the core density of NGC 288 is very low, the faint X-ray sources of NGC 288 found in the *Chandra* and *HST* observations is higher than the prediction on the basis of the collision frequency. We suggest that the CVs and chromospherically active binaries are primordial in origin, in agreement with theoretical expectation.

Subject headings: binaries: close—globular clusters: individual (NGC 288)—novae, cataclysmic variables—X-rays: binaries

1. INTRODUCTION

The number of bright X-ray sources, with luminosities greater than 10^{36} erg s⁻¹, per star has been estimated to be ~ 100 times as large in Galactic globular clusters as in the Galactic disk (Katz 1975; Clark 1975). A population of dim sources, with X-ray luminosities less than about $10^{34.5}$ erg s⁻¹, was discovered later (Hertz & Grindlay 1983; see also Verbunt 2001). The result by Pooley et al. (2003) suggests that the number of dim sources with $L_{0.5-6\text{keV}} > 4 \times 10^{30}$ erg s⁻¹ scales roughly with the number of close stellar encounters in a cluster, and that the incidence per star of dim X-ray sources is also higher in globular clusters than in the galactic disk. There is evidence, from X-ray bursts associated with the nuclear burning of accreted matter, that the bright sources are neutron stars which are accreting matter from a companion. Although some of the dim sources may be neutron stars or even black holes in quiescence, it is likely that a majority of these, especially those with the lowest luminosities, are accreting white dwarfs and X-ray active main sequence/sub-giant binaries (see e.g., Pooley et al. 2003; Verbunt & Lewin 2004; Heinke et al. 2005).

To identify faint X-ray sources in globular clusters, the *Chandra X-ray Observatory* and *Hubble Space Telescope* (*HST*) are absolutely essential because the density of X-ray sources is expected to be high and sub-arcsecond spatial resolution is required to search for reliable optical counterparts in such crowded regions. Since the launch of *Chandra*, four globular clusters dominated by faint X-ray sources have been studied in detail with *Chandra* and *HST*: 47 Tuc (Grindlay et al. 2001a; Heinke et al. 2005), NGC 6397 (Grindlay et al. 2001b), NGC 6752 (Pooley et al. 2002a), and M4 (Bassa et al. 2004). Of

these faint X-ray sources, many are believed to be cataclysmic variables (CVs) and X-ray active binaries (e.g. RS CVn and BY Dra systems). There are also quiescent low-mass X-ray binaries (qLMXBs; Heinke et al. 2003a and references therein) and millisecond pulsars (Edmonds et al. 2001; Grindlay et al. 2001b; Bassa et al. 2004).

We report here new *Chandra* and *HST* observations of the globular cluster NGC 288. NGC 288 is a globular cluster with a fairly low central density ($\log \rho_0 = 1.8 L_\odot \text{ pc}^{-3}$; Djorgovski 1993) with a core radius of 85'' and a half-mass radius of 2.25' (Trager, Djorgovski, & King 1993). The distance to this cluster is estimated at 8.4 kpc (Peterson 1993). The reddening is quite low with $E(B-V) = 0.03$, corresponding to a neutral hydrogen column $N_H = 1.6 \times 10^{20} \text{ cm}^2$ (Predehl & Schmitt 1995). NGC 288 is located close to the Southern Galactic Pole ($l = 152.28^\circ, b = -89.38^\circ$) and thus we are looking directly out of the plane. As such, there will not be many foreground objects at optical and X-ray wavelengths. The cluster center is given by Webbink (1985) as R.A.=00^h52^m45.3^s and Decl.=−26°34'43" (J2000). The absolute visual magnitude of NGC 288 is −6.7 (Harris 1996, version of February 2003). An exceptionally high concentration of blue stragglers and binary systems in the core of NGC 288 suggests that the blue stragglers' production mechanism via binary evolution can be very efficient (Bolte 1992; Bellazzini et al. 2002). In the X-ray waveband, NGC 288 has only been observed with *ROSAT HRI* (Sarazin et al. 1999). From the *ROSAT* data, only one X-ray source was within the half-mass radius (Sarazin et al. 1999).

In §2, we describe our *Chandra* observations and analysis of NGC 288. We discuss the *HST* observations in §3, and source

¹ Based on observations made with the NASA/ESA Hubble Space Telescope, obtained at the Space Telescope Science Institute, which is operated by the Association of Universities for Research in Astronomy, Inc., under NASA contract NAS 5-26555. These observations are associated with program 10120 and 9959.

² Kavli Institute for Astrophysics and Space Research, Massachusetts Institute of Technology, 77 Massachusetts Avenue, Cambridge, MA 02139; akong@space.mit.edu

³ Astronomical Institute, Utrecht University, P.O. Box 80000, 3508 TA, Utrecht, the Netherlands

⁴ Department of Astronomy, University of California, 601 Campbell Hall, Berkeley, CA 94720-3411

⁵ Department of Astronomy, University of Washington, Box 351580, Seattle, WA 98195

⁶ Space Telescope Science Institute, 3700 San Martin Drive, Baltimore, MD 21218

⁷ *Chandra* Fellow

identification in §4. A discussion and comparison with other globular clusters will be given in §5.

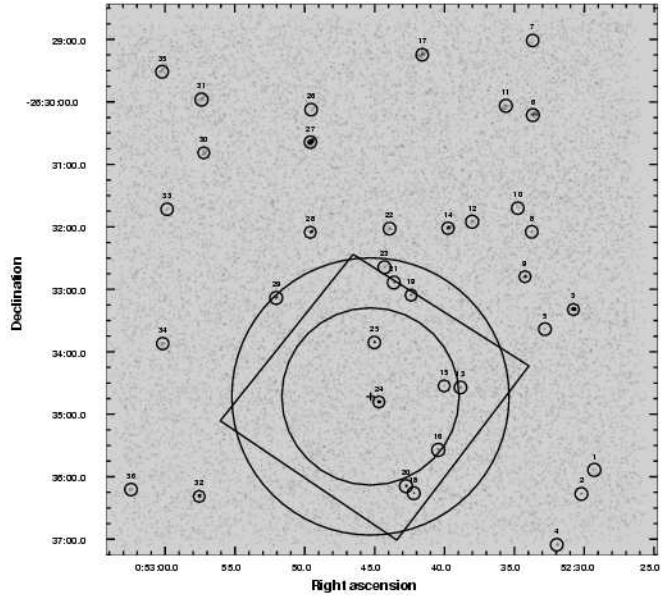


FIG. 1.—*Chandra* ACIS-S3 0.3–7 keV image of NGC 288. The image was smoothed with a Gaussian function. The large circle represents the half-mass radius and the inner circle is the core radius. The cluster center is marked by a cross. The square is the field-of-view of the *HST*/ACS. The detected X-ray sources are marked and numbered.

2. X-RAY OBSERVATIONS AND ANALYSIS

NGC 288 was observed with *Chandra* for 55 ks on 2003 February 6 (OBSID 3777). The telescope aim point is on the Advanced CCD Imaging Spectrometer (ACIS) back-illuminated S3 chip. Data were telemetered in faint mode and were collected with a frame transfer time of 3.2 s. The $\sim 8 \times 8$ arcmin 2 S3 chip covers the entire cluster half-mass radius. In this paper, we only focus on the data taken with the S3 chip.

2.1. Data Reduction

The data reduction and analysis was done with CIAO, Version 3.2.2 and ACIS Extract⁸ (Broos et al. 2002). We reprocessed the level 1 event files with CALDB 3.1.0. In order to reduce the instrumental background, only data with ASCA grades of 0, 2, 3, 4, and 6 were included. Only events with photon energies in the range of 0.3–7.0 keV were included in our analysis. We also inspected the background count rates from the S1 chip; about 6 ks was eliminated due to high background count rate (count rate > 2 counts s $^{-1}$). The effective exposure time for the observation after filtering for background flares was 49 ks.

2.2. Source Detection

Discrete sources in the *Chandra* images were found with WAVDETECT (Freeman et al. 2002) together with exposure maps. We performed source detection on the 0.3–1 keV, 1–2 keV, 2–7 keV, and 0.3–7 keV images. We set the detection threshold to be 10^{-6} , corresponding to less than one false detection due to statistical fluctuations in the background. For each of the four energy band images, we performed source detection using sequences of wavelet scales that increased by a factor of $\sqrt{2}$ from scales 1 to 16. We then combined the four source lists

into a master source list. A total of 36 X-ray sources were detected. Figure 1 shows the detected X-ray sources on the ACIS-S3 chip. Source counts in the three band passes were extracted from polygonal extraction regions which approximate 90% of the *Chandra* point spread function (PSF). Background was extracted from a circle centered on each source but excluding the 99% contour of the PSF around any point source.

Table 1 lists the 36 *Chandra* sources in our catalog, sorted in order of increasing right ascension. The columns give the source number, the position (J2000.0), the net counts in the three energy bands (soft: 0.3–1 keV; medium: 1–2 keV; hard: 2–7 keV), the 0.5–2.5 and the 0.3–7 keV unabsorbed fluxes. The conversion to fluxes assumes an absorbed power-law spectrum with a photon index of 2 and $N_H = 1.6 \times 10^{20}$ cm $^{-2}$. If we assume a thermal bremsstrahlung model with $kT = 10$ keV, then the flux will be $\sim 10\%$ higher than that of power-law model. It is worth noting that CX 15 is a very soft X-ray source with all photons coming from the 0.3–1 keV band. If we assumed a power-law model and that the counts were from the whole 0.3–7 keV range, the flux would be underestimated. Therefore, for CX 15, we convert the flux by assuming counts from 0.3–1 keV only. For the power-law model, the resulting 0.3–7 keV unabsorbed flux is 1.5×10^{-15} ergs cm $^{-2}$ s $^{-1}$. If we assume a blackbody model with $kT = 0.1$ keV, then the flux will be 7.8×10^{-14} ergs cm $^{-2}$ s $^{-1}$. The detection limit in the 0.5–2 keV band of our observation is about 3.2×10^{-16} ergs cm $^{-2}$ s $^{-1}$. We estimated the number of background sources using *Chandra* deep field data (Brandt et al. 2001). Using the log N -log S distribution derived from the deep field data, between 26–36 sources out of the 36 sources are background objects in the ACIS-S3. Within the half-mass radius, there are 11 sources and 7–9 sources are estimated to be background. For an expected number of 9 background sources, the probability of finding 11 or more background sources is 30%. Thus we cannot exclude that all our sources are background sources. Indeed, in the *Chandra* image shown in Figure 1 the surface number density is not noticeably higher within the halfmass radius than outside it.

2.3. X-ray Colors and Spectral Fitting

Many of the sources in our catalog have < 100 counts, which makes it difficult to derive spectral parameters with meaningful constraints. However, hardness ratios can give a crude indication of the X-ray spectra in these cases. We therefore computed the hardness ratios for all the detected sources. These ratios were based on the source counts in three energy bands: S (0.3–1.0 keV), M (1–2 keV), and H (2–7 keV). The two hardness ratios are defined as $HR1 = (M-S)/(M+S)$ and $HR2 = (H-S)/(H+S)$. Figure 2 shows the color-color diagram (left) and the color-magnitude diagram (right) of all X-ray sources detected in the ACIS-S3 chip. We have overlaid the color-color diagram with four lines showing the tracks followed by representative spectra with differing values of N_H . Note that the colors in the color-magnitude diagram were chosen to be consistent with previous work (e.g. Pooley et al. 2002b; Heinke et al. 2003a; Bassa et al. 2004).

We extracted the energy spectra for the brightest three X-ray sources which have $\gtrsim 200$ counts and fitted them to simple one-component spectral models including absorbed power-law and thermal bremsstrahlung models. In order to employ χ^2 statistics, all spectra were grouped into at least 15 counts per spectral

⁸ http://www.astro.psu.edu/xray/docs/TARA/ae_users_guide.html

TABLE 1
Chandra SOURCE PROPERTIES

Name	Source CXOU J	R.A. (J2000.0)		Decl. (J2000.0)		Net Counts			$f_{0.5-2.5}$	$f_{0.3-7}$	Counterpart
		Soft	Medium	Hard							
CX 1	005229.4-263553	00:52:29.413 (0.30)	-26:35:53.46 (0.23)	0.7	4.8	0.5	0.46	0.91			
CX 2	005230.3-263616	00:52:30.336 (0.21)	-26:36:16.52 (0.23)	1.7	2.8	2.6	0.54	1.07			
CX 3	005230.9-263319	00:52:30.909 (0.07)	-26:33:19.47 (0.04)	98.7	69.8	28.5	15.16	29.85			
CX 4	005232.0-263705	00:52:32.092 (0.12)	-26:37:05.36 (0.18)	0.9	11.0	5.9	1.37	2.7			
CX 5	005232.9-263338	00:52:32.950 (0.22)	-26:33:38.28 (0.09)	1.8	2.8	2.6	0.56	1.09			
CX 6	005233.8-263012	00:52:33.818 (0.24)	-26:30:12.67 (0.23)	22.7	27.2	7.4	4.43	8.68			
CX 7	005233.8-262901	00:52:33.838 (0.26)	-26:29:01.05 (0.68)	4.8	5.9	5.5	1.26	2.45			
CX 8	005233.8-263204	00:52:33.899 (0.28)	-26:32:04.80 (0.21)	4.5	0.0	5.3	0.76	1.48			
CX 9	005234.3-263247	00:52:34.380 (0.09)	-26:32:47.90 (0.09)	12.7	12.8	9.6	2.71	5.31			
CX 10	005234.8-263142	00:52:34.897 (0.39)	-26:31:42.08 (0.25)	2.4	1.6	4.1	0.33	1.22			
CX 11	005235.7-263003	00:52:35.748 (0.40)	-26:30:03.80 (0.14)	15.7	7.2	1.1	1.86	3.64			
CX 12	005238.1-263155	00:52:38.162 (0.19)	-26:31:55.14 (0.11)	1.6	0.0	13.3	1.14	2.25			
CX 13	005238.9-263434	00:52:38.991 (0.13)	-26:34:34.29 (0.09)	0.0	0.0	7.7	0.60	1.17	<i>HST</i>		
CX 14	005239.8-263201	00:52:39.888 (0.11)	-26:32:01.33 (0.08)	9.7	15.8	13.5	3.02	5.91			
CX 15	005240.1-263432	00:52:40.164 (0.23)	-26:34:32.82 (0.17)	3.9	0.0	0.0	0.32 ^a , 0.78 ^b	0.78 ^a , 1.54 ^b	<i>HST</i>		
CX 16	005240.5-263534	00:52:40.585 (0.18)	-26:35:34.32 (0.13)	2.9	4.9	4.8	0.97	1.91			
CX 17	005241.7-262914	00:52:41.735 (0.23)	-26:29:14.74 (0.26)	25.4	25.3	13.9	5.01	9.83			
CX 18	005242.3-263615	00:52:42.337 (0.10)	-26:36:15.83 (0.15)	0.0	6.9	3.8	0.83	1.62	<i>HST</i>		
CX 19	005242.5-263305	00:52:42.526 (0.14)	-26:33:05.71 (0.13)	2.9	8.9	2.8	1.12	2.21	<i>HST</i>		
CX 20	005242.6-263609	00:52:42.622 (0.08)	-26:36:09.08 (0.08)	8.9	8.9	7.8	1.97	3.89	<i>HST</i>		
CX 21	005243.7-263253	00:52:43.764 (0.12)	-26:32:53.54 (0.12)	3.9	6.9	0.0	0.83	1.63			
CX 22	005244.0-263201	00:52:44.070 (0.22)	-26:32:01.78 (0.16)	8.7	3.8	1.5	1.08	2.12			
CX 23	005244.4-263238	00:52:44.435 (0.18)	-26:32:38.88 (0.11)	1.9	1.9	1.7	0.43	0.83			
CX 24	005244.8-263448	00:52:44.832 (0.03)	-26:34:48.22 (0.03)	29.9	99.9	71.8	15.64	30.56	<i>HST, ROSAT</i>		
CX 25	005245.1-263351	00:52:45.158 (0.10)	-26:33:51.08 (0.06)	11.9	15.9	7.8	2.76	5.40	<i>HST</i>		
CX 26	005249.6-263007	00:52:49.682 (0.25)	-26:30:07.47 (0.44)	0.0	1.4	11.2	0.97	1.91			
CX 27	005249.7-263038	00:52:49.731 (0.06)	-26:30:38.63 (0.05)	184.2	210.5	102.9	38.50	75.45			
CX 28	005249.7-263205	00:52:49.744 (0.11)	-26:32:05.28 (0.09)	2.7	16.8	19.5	3.02	5.91			
CX 29	005252.1-263308	00:52:52.184 (0.10)	-26:33:08.26 (0.12)	0.0	6.9	16.6	1.81	3.55			
CX 30	005257.3-263048	00:52:57.360 (0.18)	-26:30:48.93 (0.20)	2.2	11.4	12.6	2.03	3.97			
CX 31	005257.5-262957	00:52:57.519 (0.28)	-26:29:57.76 (0.24)	10.5	11.8	3.8	2.01	3.96			
CX 32	005257.7-263618	00:52:57.700 (0.08)	-26:36:18.90 (0.11)	42.8	5.9	0.6	3.80	7.47			
CX 33	005259.9-263143	00:52:59.980 (0.34)	-26:31:43.10 (0.27)	2.4	2.5	3.5	0.65	1.26			
CX 34	005300.3-263352	00:53:00.307 (0.19)	-26:33:52.12 (0.15)	0.0	5.7	7.4	1.02	1.99			
CX 35	005300.3-262931	00:53:00.341 (0.43)	-26:29:31.06 (0.45)	2.1	11.7	12.4	2.01	3.97			
CX 36	005302.5-263612	00:53:02.583 (0.33)	-26:36:12.27 (0.20)	0.7	5.8	3.4	0.77	1.50			

NOTES. — The positions in the table have been corrected for boresight, in that the right ascensions and declinations resulting from the Chandra source detection with *wavdetect* have been corrected by 0.137" and -0.055" respectively (see Sect. 3.2). The positional uncertainties are in units of arcsec given by *wavdetect*. The unabsorbed flux is in units of 10^{-15} ergs cm $^{-2}$ s $^{-1}$ and is derived assuming a power-law model (except for CX 15) with $N_H = 1.6 \times 10^{20}$ cm $^{-2}$ and a photon index of 2.

^a Assuming a blackbody model with 0.1 keV and counts from 0.3–1 keV.

^b Assuming a power-law model with photon index of 2 and counts from 0.3–1 keV.

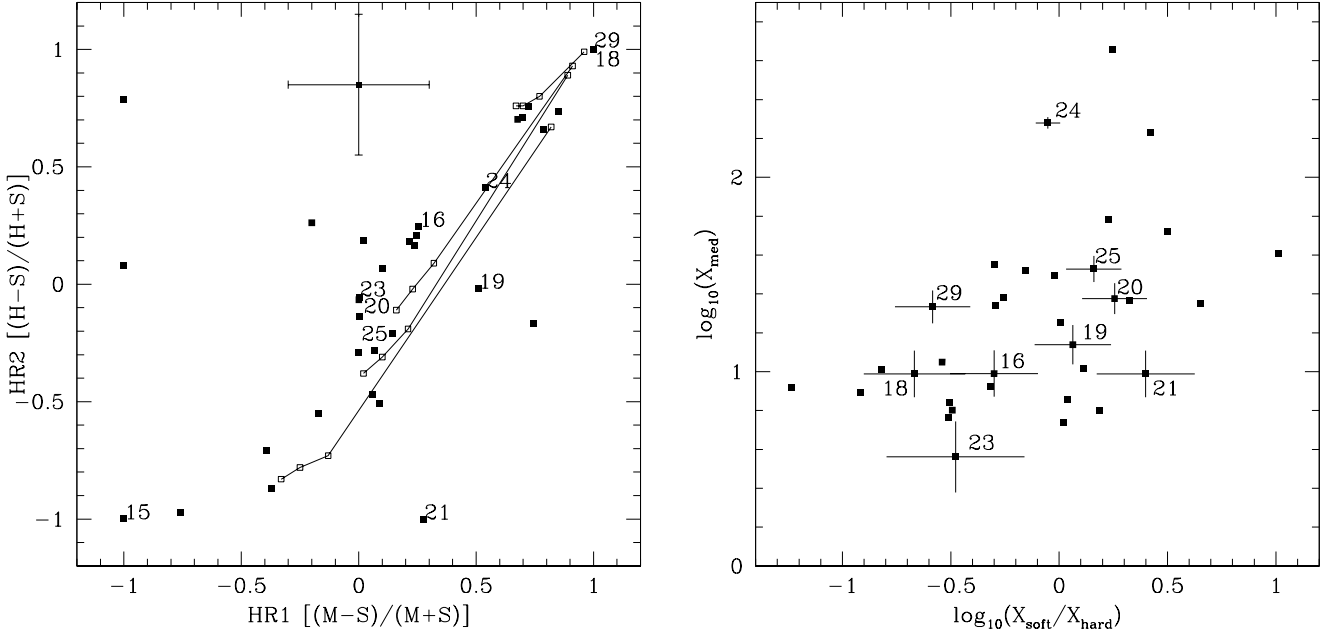


FIG. 2.— Left: X-ray color-color diagram of *Chandra* sources in NGC 288. The number corresponds to the source number inside the half-mass radius. Also plotted are the hardness ratios estimated from different spectral models. Top to bottom: Blackbody model with $kT = 1$ keV, thermal bremsstrahlung model with $kT = 5$ keV, power-law model with $\alpha = 2$, and 3. For each model, N_H (open squares) varies from the left as 1.6×10^{20} , 5×10^{20} , 10^{21} , and 10^{22} cm $^{-2}$. Right: X-ray color-magnitude diagram of NGC 288. The X-ray color is defined as the logarithm of the ratio of 0.5–1.5 keV (X_{soft}) counts to 1.5–6 keV (X_{hard}) counts, and the magnitude is the logarithm of 0.5–4.5 keV (X_{med}) counts. Sources within the half-mass radius are marked with error bars.

bin. We forced N_H to be $\geq 1.6 \times 10^{20}$ cm $^{-2}$, the cluster N_H derived from optical studies. All spectra can be fitted equally well with both models. Table 2 summarizes the spectral fits. For CX 3, the N_H converged to values much lower than the cluster N_H derived from optical studies. For the other two sources, the N_H of the thermal bremsstrahlung model is slightly higher than the cluster value, while it is much higher for power-law model. The temperatures of the thermal bremsstrahlung model vary between 1.7 and 7 keV, while the photon index of the power-law model is consistent with 2.

3. OPTICAL OBSERVATIONS

NGC 288 was observed with *HST* Advanced Camera for Surveys (ACS) on 2004 September 20 (Proposal ID: 10120). The observations consist of deep F435W (B_{435}), F625W (r_{625}), and F658N ($H\alpha_{658}$) images covering the core of the cluster. The exposure time with the F435W, F625W, and F658N filters is 740s, 320s, and 1760s, respectively. The ACS field-of-view covers the entire core radius of the cluster and about 73% of the half-mass radius (see Figure 1). Three X-ray sources (CX16, 18 and 20) coincide with an archival *HST* Wide Field and Planetary Camera 2 (WFPC2) observation of NGC 288. For this observations, the F255W (nUV_{255}), F336W (U_{336}), F555W (V_{555}) and F814 (I_{814}) filters were used. Exposure times were 700 s in F255W, 3760 s in F336W, 430 s in F555W and 585 s in F814W.

3.1. Data Reductions and Photometry

Images of each bandpass were shifted and co-added using the MultiDrizzle package in PyRAF, with masking of cosmic rays, saturated pixels, and bad pixels. We used the combined images for correcting astrometry and identifying optical counterparts of X-ray sources in the cluster. Figure 3 shows the

⁹ <http://purcell.as.arizona.edu/~andy/dolphot/>

color *HST* ACS image of NGC 288. However, we used individual images to perform PSF photometry with the DOLPHOT package that is adapted from HSTphot (Dolphin 2000) for the use of ACS data⁹. DOLPHOT is a stand-alone package to perform PSF photometry with a module for ACS data. We did not use the combined images for photometry because drizzled images require re-sampling producing suboptimal photometry. DOLPHOT can be run on multiple images of the same field and outputs the combined photometry for each filter. We first applied *acsmask* to mask bad pixels according to the data quality image provided by STScI. We then used *calcsky* to create sky images for background determination. Finally, we performed PSF photometry using DOLPHOT with lookup tables for the ACS PSF and produced a master list of positions and magnitudes for each star found. The final magnitudes were corrected for aperture and charge transfer efficiency effects. Additional selection criteria were applied to eliminate cosmic rays, artifacts, and “stars” lying on the diffraction spikes of the very brightest stars. The final photometry data were used to construct the color-magnitude diagrams (CMDs) shown in Figure 4. Stars are shown if they appear in all three filters.

The archival *HST*/WFPC2 observation was photometered using HSTphot 1.1.5b (Dolphin 2000, see Bassa et al. 2004 for a more detailed description).

3.2. Astrometry

To identify optical counterparts to the *Chandra* X-ray sources in the field, we have to improve the astrometry of both datasets. We retrieved a 5-minute *V*-band image of NGC 288 with the Wide Field Imager (WFI) at the ESO 2.2 meter telescope on La Silla, taken on 2004 June 14 and used that to

calibrate the *HST*/ACS images. The WFI has an array of 8 CCDs, each CCD having a $8' \times 16'$ field of view, giving a total of $33' \times 34'$. An $8' \times 8'$ subsection of the WFI chip covering the cluster center was used that contained 93 UCAC2 standards (Zacharias et al. 2004). Of these, 72 were not saturated and appeared stellar and unblended. Fitting for a 6 parameter transformation, we obtained a solution giving residuals of $0.056''$ in R.A. and $0.059''$ in Decl.

The astrometry of the WFI image was then transferred to the two ACS/WFC chips (WFC1 and WFC2). We used DOLPHOT to generate positions and photometry for all stars on the ACS/WFC chips. These positions were corrected for the considerable geometric distortion using polynomials (Hack & Cox 2001). A selection of the stars on each chip (having $r_{625} < 18.0$) were matched against stars on the WFI image, where we used the distortion corrected positions of ACS/WFC for comparison with the calibrated position on the WFI. For WFC1, 174 stars were selected and outliers were removed through an iterative process. The astrometric solution converged using 147 stars, yielding residuals of $0.016''$ in R.A. and $0.018''$ in Decl. For WFC2, we started off with 206 stars, while the final solution has 155 stars with residuals of $0.014''$ in R.A. and $0.016''$ in Decl.

For the astrometric calibration of the archival *HST*/WFPC2 images, we first corrected all pixel positions of the stars for distortion and placed them on a common frame using the distortion corrections and relative chip positions and offsets by Anderson & King (2003). The resulting positions were matched to those of stars on the WFI image, where the final astrometric solution used 207 stars giving residuals of $0.022''$ in RA and $0.024''$ in Decl.

TABLE 2

SPECTRAL FITS OF THE BRIGHTEST SOURCES

CX	Model ^a	N_H ^b	kT/α	χ^2_ν/dof	$f_{0.3-7}^c$
3	TB	$1.6^{+3.4}_{-0.9}$	$1.7^{+0.9}_{-0.5}$	1.3/10	22.0
	PL	$1.6^{+6.4}_{-0.9}$	$2.1^{+0.6}_{-0.2}$	1.1/10	28.0
24	TB	$3.0^{+1.4}_{-1.1}$	$7.0^{+21.3}_{-3.4}$	0.9/10	48.0
	PL	$35^{+1.9}_{-1.1}$	$1.7^{+0.4}_{-0.3}$	0.9/10	36.0
27	TB	$3.9^{+3.1}_{-2.2}$	$4.4^{+2.4}_{-1.4}$	1.0/28	82.0
	PL	$8.4^{+4.0}_{-4.0}$	$1.9^{+0.2}_{-0.2}$	0.9/28	96.0

NOTES. — All quoted uncertainties are 90%.

^a TB: thermal bremsstrahlung; PL: power-law.

^b in units of 10^{20} cm^{-2}

^c 0.3–7 keV unabsorbed flux in units of $10^{-15} \text{ ergs cm}^{-2} \text{ s}^{-1}$.

For the *Chandra* image, we first used the Aspect Calculator¹⁰ provided by the *Chandra* X-ray Center to correct the aspect offset. This will provide an absolute astrometry of $0.6''$ (90%). The shifts were small: $0.07''$ in right ascension and $0.03''$ in declination. Inspection of the 99% confidence error circles of the *Chandra* X-ray sources (using the positions from Table 1) on the WFI image yields several likely counterparts. X-ray sources CX 3, CX 12, CX 28, CX 30 appear to coincide with stellar objects, whereas CX 7, CX 8, CX 17, CX 22, CX 26, CX 32, CX 36 appear to coincide with extended objects, possibly background galaxies. Based on brightness, positional accuracy, and conformity of the image to the point spread function CX 28 and CX 30 are the most promising stellar counterparts. In addition, CX 28 and CX 30 are outside the half-mass radius, hence the stellar density from the cluster is relatively low implying a low probability of chance coincidences. Based on these two

optical counterparts, the boresight correction that needs to be applied to the X-ray source positions is $0.137 \pm 0.104''$ in R.A. and $-0.055 \pm 0.096''$ in Decl.

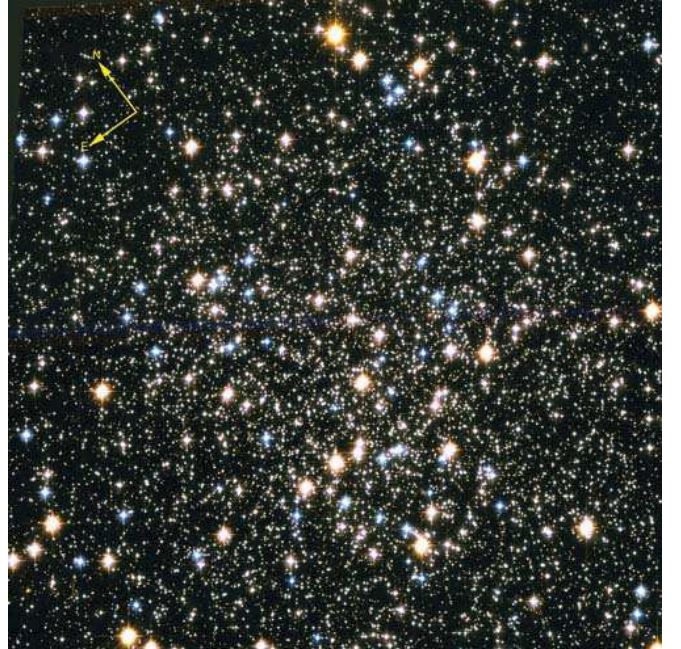


FIG. 3.— True color *HST* ACS image (202×202 arcsec) of NGC 288 core. This was constructed by combining all the r_{625} (red), $0.5(B_{435} + r_{625})$ (green), and B_{435} (blue) images.

4. SOURCE IDENTIFICATION AND CLASSIFICATION

To obtain optical identifications for the X-ray sources, we use the precise astrometry described in the previous sections. We searched for optical counterparts within the 95% *Chandra* error circle which is the quadratic sum of the positional uncertainty for the X-ray source, the uncertainty in the optical astrometry (UCAC2 to WFI astrometry and WFI to *HST*/ACS astrometry), and the uncertainty in the X-ray boresight correction. Within the ACS field-of-view, there are nine *Chandra* sources and we suggest optical counterparts based on positional coincidence alone to seven of them. In case of multiple sources inside the error circle, we included all the candidates within the 95% X-ray error circle. The results of each candidate optical counterpart are summarized in Table 3, and finding charts are shown in Figure 5. Using the photometric data from the *HST* ACS, we constructed CMDs, shown in Figure 4.

To help in assessing the nature of the optically identified sources, we show in Figure 6 the X-ray luminosity as a function of the absolute magnitude, for low-luminosity X-ray sources in globular clusters. The large symbols in this figure indicate the X-ray sources with possible optical counterparts, in the field of view of our *Chandra* observation of NGC 288, the smaller symbols show objects found in other clusters, mostly 47 Tuc and M4 (see Bassa et al. 2004). We note that the absolute magnitudes and X-ray luminosities for the sources in our NGC 288 observations are computed under the assumption, which we will test below, that they are associated with NGC 288. As discussed earlier, we caution that the *Chandra* deep field data imply that for the 11 X-ray sources within the half-mass radius, there is a 30% probability that *all* of them are background sources.

¹⁰ http://cxc.harvard.edu/ciao/threads/arcsec_correction/

TABLE 3
OPTICAL COUNTERPARTS TO *Chandra* X-RAY SOURCES

CX	Δ R.A. (arcsec)	Δ Decl. (arcsec)	U_{336}	B_{435}	V_{555}	r_{625}	I_{814}	$H\alpha_{658}$	f_X/f_r^a	Classification ^b
13a	0.09	-0.31		24.96 ± 0.04		22.90 ± 0.02		22.58 ± 0.05	0.8	AB?
13b	0.42	-0.08		26.04 ± 0.09		22.86 ± 0.02		22.34 ± 0.04	0.76	CV? AGN?
15	-0.27	0.19		26.81 ± 0.17		25.78 ± 0.19		25.15 ± 0.74	11.6	AGN
18	-0.10	-0.26	22.71 ± 0.08	22.73 ± 0.01	21.79 ± 0.02	21.52 ± 0.01	20.78 ± 0.02	21.16 ± 0.02	0.3	AB
19a	0.31	0.007		25.24 ± 0.05		25.33 ± 0.11		23.86 ± 0.12	13.7	AGN
19b	-0.55	-0.21		20.54 ± 0.004		19.73 ± 0.004		19.50 ± 0.013	0.08	AB
20a	-0.1	0.09		27.51 ± 0.29		26.37 ± 0.27		24.78 ± 0.42	60.1	AGN
20b	0.16	-0.03		25.42 ± 0.06	24.34 ± 0.15	24.19 ± 0.05	22.88 ± 0.08	23.74 ± 0.12	8.6	CV
24	-0.17	0.007		24.88 ± 0.04		23.58 ± 0.04		23.47 ± 0.10	39.7	CV
25	0.30	-0.05		26.92 ± 0.19		25.70 ± 0.23		24.05 ± 0.19	48.1	AGN

Note — The last column give a tentative classification; for the sources with two possible optical counterparts, this classification holds only for the actual counterpart.

^a Ratio of X-ray to optical (r_{625}) flux, using $\log(f_X/f_r) = \log f_X + 5.67 + 0.4r_{625}$ (Green et al. 2004); f_X is derived in the 0.3–7 keV band.

^c CV: cataclysmic variable; AB chromospherically active binary; AGN: active galactic nuclei

We first consider the X-ray sources with only one suggested counterpart in the error circle. The ratio of the X-ray to optical flux locates CX 18 in the region of active binaries in Figure 6, albeit close to the boundary with CVs. The star in the error circle of CX 18 is located on the main-sequence in the CMD of Figure 4. Because it does not show noticeable $H\alpha$ emission, is on the main sequence in $U_{336} - V_{555}$, and is not detected in the near ultraviolet, it is unlikely to be a CV, and we suggest that CX 18 is a chromospherically active binary.

The candidate cluster counterpart to CX 24 is blue with respect to the main sequence, and has no $H\alpha$ emission, being located rather on the main sequence in the $H\alpha$ diagram (Figure 4). It has a high X-ray to optical flux ratio and a hard spectrum with 0.3–7 keV luminosity of $\sim 4 \times 10^{32}$ ergs s $^{-1}$. It is worth noting that CX 24 is the only X-ray source in the half-mass radius detected with *ROSAT* (Sarazin et al. 1999). Using the *Chandra* spectral fit, the X-ray luminosity during the *ROSAT* observations is about 10^{33} ergs s $^{-1}$, a factor of 2.5 higher than our *Chandra* observation. We suggest that CX 24 is a CV, even though its $H\alpha$ emission does not appear to be strong.

The sources CX 15 and CX 25 are optically extended, and thus almost certainly background galaxies. Indeed, if we compute their X-ray luminosity and optical magnitude under the wrong assumption that they are in NGC 288, we find that they are located in the $L_x - M_V$ diagram in an area where no genuine cluster sources have been found. A probable background quasar in the *Chandra* field of view of our M 4 observation is in the same location of Figure 6 (for the wrong assumption that it belongs to the cluster M 4; Bassa et al. 2004, 2005; Bedin et al. 2003).

Turning now to the sources with more than one possible counterpart in the error circle, we first note that our suggested classifications depend on the optical object indeed being the counterpart. One star in the error circle of CX 13, CX 13a, is on the main sequence both in the CMD and in the $H\alpha - r$ diagram. Like CX 18, it may be an active binary. The other star, CX 13b is redder than the main sequence. Its X-ray to optical flux ratio is somewhat high for an active binary. Possibly it is an (obscured?) active galaxy. Alternatively, its red color could be an artifact of variation of its blue magnitude, in which case it may be a CV. (Note that we have no evidence for such variation.) In the absence of more information, a secure classification of CX

13 thus is not possible.

Of the two objects in the error circle of CX 19, the brighter one (CX 19b) would a priori be the more probable counterpart, since the probability of a chance coincidence is higher for the more numerous faint objects. Its colors (Figure 4) and X-ray to optical flux ratio (Figure 5) then suggests that CX 19b is a chromospherically active binary. If the fainter object CX 19a is the counterpart, its X-ray to optical flux ratio (Figure 5) suggests that it is a background galaxy/AGN.

The brighter object in the error circle of CX 20, CX 20b is blue, and has a relatively high X-ray to optical flux ratio (Figure 6): it may be a CV. CX 20b was also imaged by WFPC2 with the V_{555} and I_{814} filters. It has $V_{555} = 24.34$ and is on the main-sequence in $V - I$ (similar to CVs in other clusters, e.g. NGC6397 and 47 Tuc; Cool et al. 1998, Edmonds et al. 2003). On the other hand, CX 20a is extended, and therefore an galaxy, an active galaxy when it is the counterpart of CX 20. CX 20a is below the detection limit in the archival WFPC2 observations.

There are two unidentified X-ray sources (CX 16 and CX 21) in the ACS field-of-view. CX 16 is in between two bright stars and the spikes produced by these bright stars prevent us from searching for any faint optical sources inside the *Chandra* error circle. The region of CX 16 was also observed with the WFPC2, but neither do we find a counterpart inside the *Chandra* error circle in these data. CX 21 is near the edge of the field and part of the *Chandra* error circle is in the dithering pattern of the image. Therefore the sensitivity is greatly reduced. Two additional sources (CX 23 and CX 29) are inside the half-mass radius but were not observed with *HST*. In any case, if the identifications of CX 18 and CX 24 are correct, then these two remaining sources are very likely part of the extra-galactic background.

In summary, we find one good candidate CV (CX 24) and the source is already detected with *ROSAT* (Sarazin et al. 1999), and one good candidate active binary (CX 18). The X-ray to optical luminosity ratio of CX 24 is in the upper range of the values observed for CVs in globular clusters so far, and the X-ray to optical luminosity ratio of CX 18 is amongst the highest observed so far for active binaries in globular clusters. In addition to these, we have possible cluster members and according classifications in the error circles of CX 13 (active binary or CV), CX 19 (active binary) and CX 20 (CV).

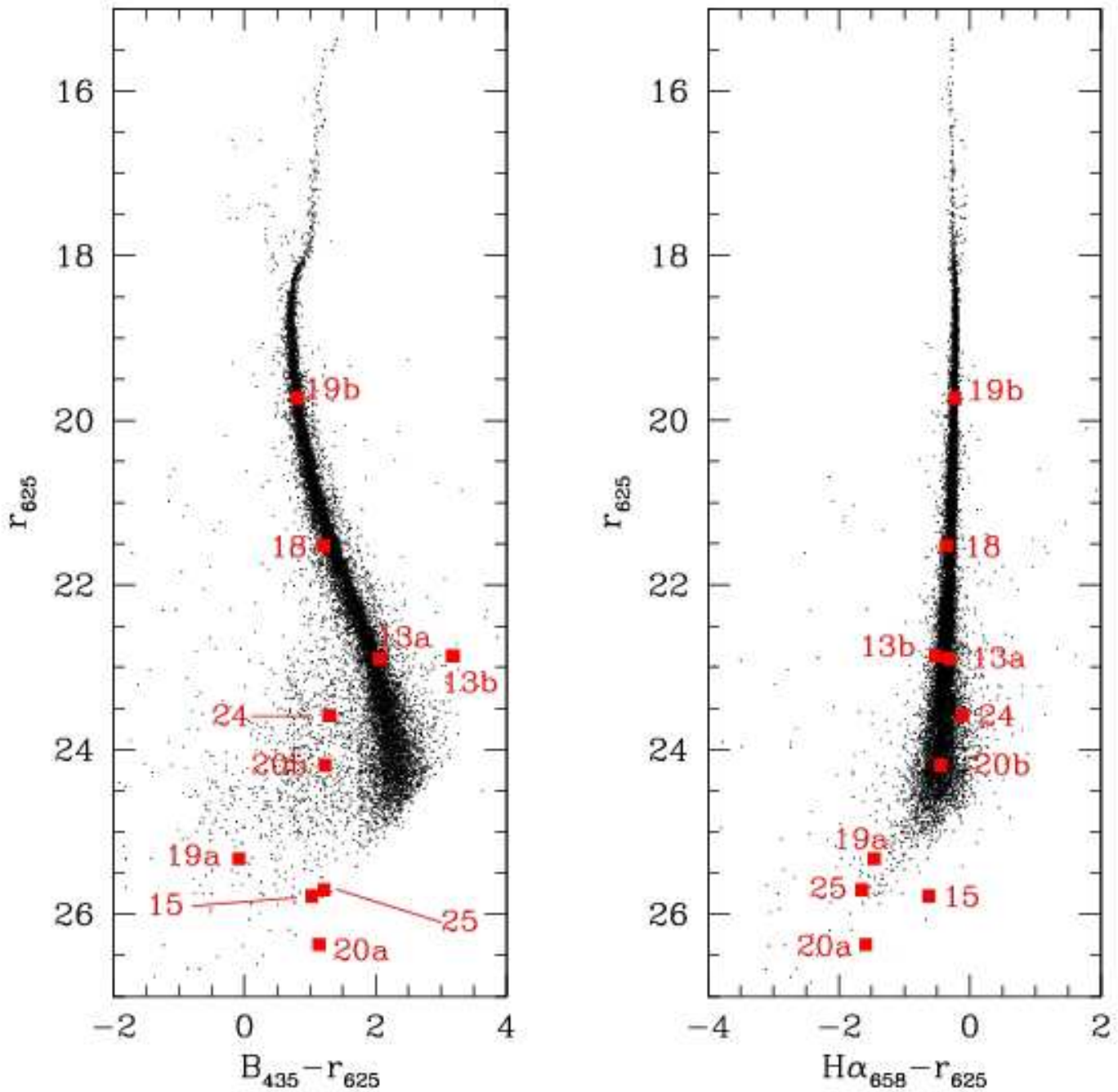


FIG. 4.— Color-magnitude diagram of the *HST* ACS observations of NGC 288. The numbers refers to the candidate optical counterparts to the X-ray sources.

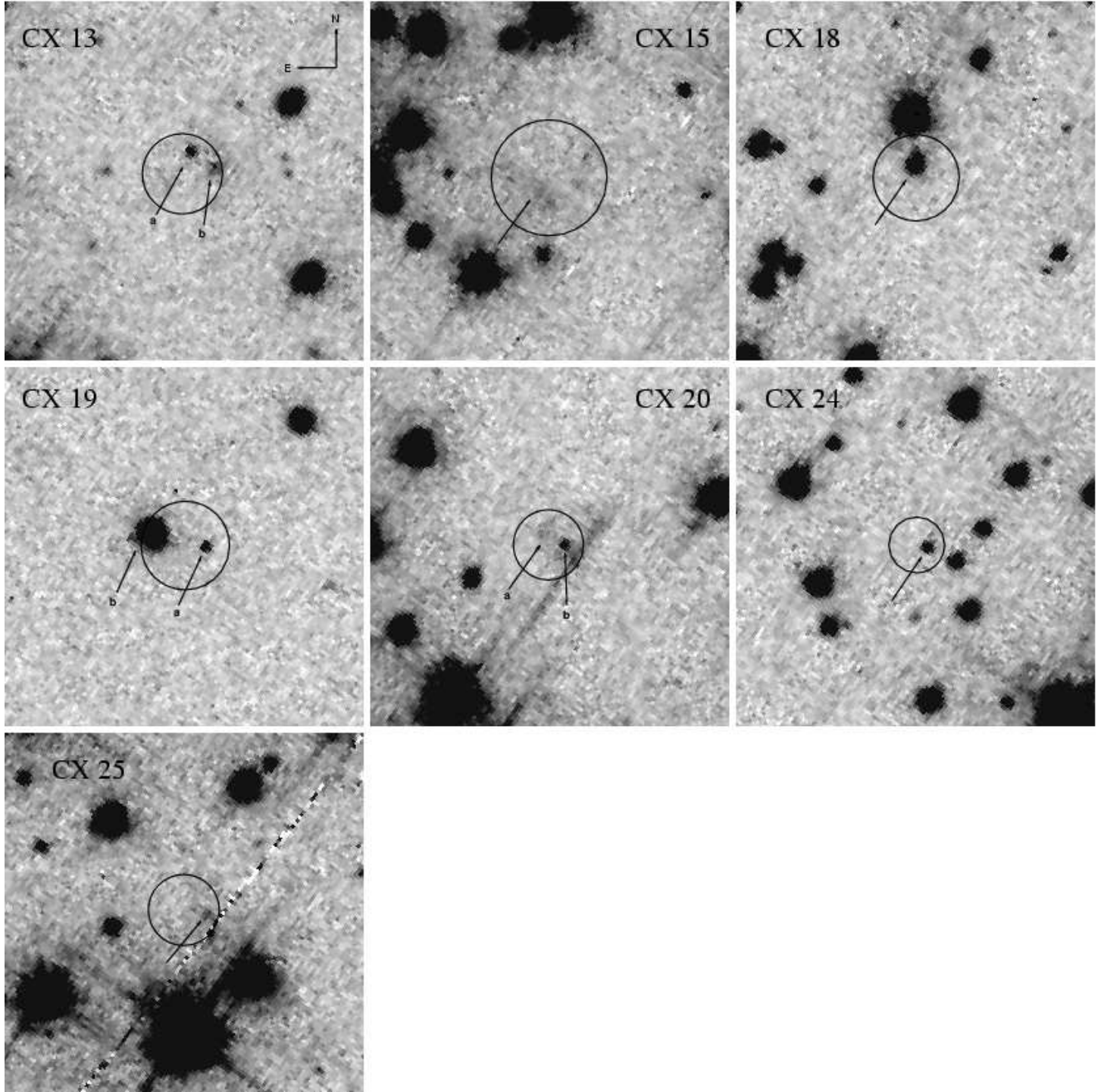


FIG. 5.— $5'' \times 5''$ finding charts for the candidate optical counterparts, obtained from *HST* ACS observations. These images were taken in B_{435} . We have overlaid the 95% error circles for the *Chandra* source positions and the candidate stars themselves are indicated by arrows. All images have the same grey scale.

Lastly, we consider all the remaining *Chandra* sources outside the half-mass radius; we do not possess useful optical data for any of these. Statistically we do not expect any of the sources outside the half-mass radius to be associated with NGC 288 (see Section 2.2). From the *Chandra* deep field data, for the entire ACIS-S3 chip field of view, we expected that 0–10 sources are associated with NGC 288. If CX 18 and CX 24 (or indeed additionally CX 13, CX 19 and CX 20) are CVs or chromospherically active binaries (hence cluster members), then there are at most eight (five) additional X-ray sources associated with NGC 288. In the absence of information of the optical colors of the counterparts, it is not possible to pursue this question further for individual cases. Nevertheless, we here describe the X-ray properties, *assuming cluster membership*. The X-ray fluxes of all *Chandra* sources are listed in Table 1 and 2, and the luminosities (assuming 8.4 kpc) range from 7×10^{30} to 8×10^{32} ergs s $^{-1}$. CX 3 is one of the three brightest X-ray sources. It has a relatively soft spectrum (see Table 2) and is therefore inconsistent with a CV. It could be either a qLMXB or, of course, yet another background galaxy. In contrast, the brightest source, CX 27, has a hard spectrum, favouring a CV identification; it is also noteworthy as an X-ray variable; the *Chandra* spectrum indicates that it has a 0.3–7 keV flux of $8–9 \times 10^{-14}$ ergs cm $^{-2}$ s $^{-1}$, but the source was not detected with *ROSAT* with a detection limit of 6×10^{-14} ergs cm $^{-2}$ s $^{-1}$. Excluding the brightest three sources (CX 3, CX 24 and CX 27), the remainder have luminosities $< 10^{32}$ ergs s $^{-1}$ with an average of 3×10^{31} ergs s $^{-1}$. This luminosity is at the lower end of quiescent neutron stars in the field. Moreover, the X-ray colors are harder than for neutron star systems. Hence, the remaining lower-luminosity X-ray sources outside the half-mass radius are very unlikely to be quiescent neutron stars. Of these, the X-ray luminosities of CX 6, and CX 17 are too high for any chromospherically active binary, and their relatively hard X-ray colors would indicate that they are probably CVs, or absorbed AGN.

5. DISCUSSION

The luminosities of both good candidate members, CX24 and CX18, as well as those of the three less secure members CX13, CX19 and CX20, are above the lower limit of 4×10^{30} ergs s $^{-1}$ in the 0.5 – 6.0 keV range used in the study by Pooley et al. (2003) into the relation between the stellar encounter rate and the incidence of X-ray sources in globular clusters. To see whether NGC 288 fits this relation we compare its collision number $\Gamma \equiv \rho_o^{1.5} r_c^2$ (Verbunt 2003) with those of some other clusters, using the parameters listed in Table 4. Here ρ_o is the central density of the cluster, and r_c the core radius. The encounter number for NGC 288 is about 650 times smaller than that of 47 Tuc, and 30 times smaller than that of M 4. Pooley et al. (2003) reports 41 ± 2 sources above the lower luminosity limit in 47 Tuc (see also Grindlay et al. 2001a; the uncertainty is due to the estimated number of background sources), and thus, if the number of sources scales with the encounter rate, the presence of two to five sources in NGC 288 is a very significant overabundance, even if we take into account small number errors due to Poissonian fluctuations. The same conclusion is reached on the basis of comparison with M 4. This indicates that the sources in NGC 288 are not formed via stellar encounters.

Indeed, for magnetically active binaries, an origin from a primordial binary is much more likely (Verbunt 2002). A scaling with the total mass of the cluster is expected in this case, pro-

vided that no large numbers of binaries have been destroyed by close encounters. In a low-density cluster like NGC 288, no such large scale destruction has taken place. Since our information on low-luminosity X-ray sources in most clusters is limited to the region within the half-mass radius, we compare also the masses within this radius. By definition, however, these masses are half of the total mass, and thus the scaling between clusters is the same as for the total mass. If the visual mass-to-light ratio is the same for all clusters listed in Table 4, the half masses scale with $10^{-0.4M_V}$. Thus the half-mass radii of NGC 6397 and NGC 288 contain about 20% less mass than the half-mass radius of M 4, which in turn contains a factor 10 less mass than the half-mass radius of 47 Tuc. Scaled by mass, the predicted number of active binaries $L_{0.5-6\text{keV}} > 4 \times 10^{30}$ erg s $^{-1}$ in NGC 288 should be similar to those in NGC 6397 and M 4, and about one tenth of those in 47 Tuc. This is indeed observed.

We consider this strong evidence that magnetically active binaries in globular clusters evolve from primordial binaries, much strengthening the conclusion based by Bassa et al. (2004) on the source numbers in M 4.

As argued by Verbunt (2002), CVs take a position in between low-mass X-ray binaries with a neutron star or black hole, which are certainly formed from close encounters, and the magnetically active binaries, formed from primordial binaries. The scaling of source number with encounter number found for the sources with $L_{0.5-6\text{keV}} > 4 \times 10^{30}$ ergs s $^{-1}$ by Pooley et al. (2003; see also Heinke et al. 2003b) suggests that CVs are mostly made via stellar encounters as well. This is in agreement with the result by Davies (1997) that the formation of CVs via evolution from – relatively wide – primordial binaries is suppressed by the destruction of such binaries in dense cores of globular clusters. We do not expect even a single CV in NGC 288 if we scale with encounter numbers from any of the other clusters listed in Table 4. However, neither the observed scaling law nor the theoretical computations extends to clusters with core densities or encounter rates as low as that of NGC 288. According to the computations by Davies (1997) a cluster core with a star density of 1000 pc $^{-3}$ allows most of the CV progenitors to evolve into a CV. It is therefore probable that the CV, CX 24, in cluster with an even lower central number density, evolved from a primordial binary. As an even more extreme case than NGC 288, recent *Chandra* observation of the old open cluster M 67 reveals a large number of BY Dra and RS CVn systems as well as interacting binary candidates (van den Berg et al. 2004). It is interesting to note that the total X-ray luminosity of M 67 is dominated by binaries with giants, whereas no such binaries have been securely identified as optical counterpart to an X-ray source in any globular cluster so far. Investigations of other globular clusters with low density cores must be done to verify these conclusions.

TABLE 4
SCALING PARAMETERS OF M 4, NGC 6397, 47 TUC AND NGC 288

Cluster	$\log \rho_0$ ($L_\odot \text{ pc}^{-3}$)	r_c ($''$)	d (kpc)	M_V	Γ	M_h
M 4	4.01	49.8	1.73	-6.9	1.0	1.0
NGC 6397	5.68	3.0	2.3	-6.6	2.1	0.76
47 Tuc	4.81	24.0	4.5	-9.4	24.9	10
NGC 288	1.80	85.0	8.4	-6.7	0.03	0.83

Values for central density (ρ_0), core-radius (r_c), distance (d) and absolute visual magnitude (M_V) originate from Harris 1996 (version of February 2003). For M4, the values of ρ_0 and M_V are computed for the distance and reddening of Richer et al. (1997). The collision number is computed from $\Gamma \propto \rho_0^{1.5} r_c^2$ and the half-mass from $M_h \propto 10^{-0.4M_V}$. Values for Γ and M_h are normalized to the value of M4.

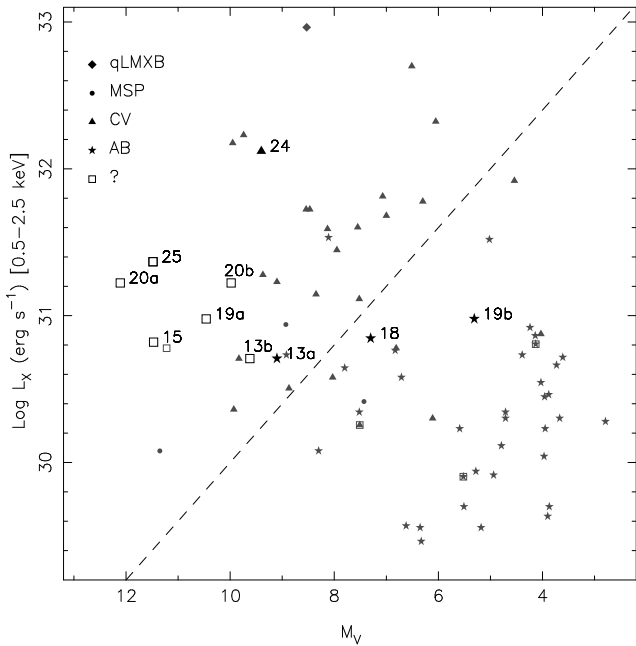


FIG. 6.— X-ray luminosity as a function of the absolute magnitude, for low-luminosity X-ray sources in globular clusters. The large symbols in this Figure indicate the optically identified X-ray sources in the field of view of our Chandra observation of NGC 288, where we compute absolute magnitude and X-ray luminosity under the assumption that the sources are cluster members. This assumption is probably correct for the candidate CV (large triangle) and the three candidate active binaries (large stars); the sources indicated with a large square are probably extragalactic sources. The smaller symbols in this Figure indicate objects found in other clusters, mostly 47 Tuc and M4 (see Figure 6 of Bassa et al. 2004). Since we do not have observations of NGC 288 in the V-band, we estimate V from $V = 0.5(B_{435} + r_{625})$. The dashed line of constant X-ray to optical flux ratio roughly separates CVs from active binaries.

We thank Andrew Dolphin for providing a modified version of his DOLPHOT code. Support for Proposal number 10120 and 9959 was provided by NASA through a grant from the Space Telescope Science Institute, which is operated by the Association of Universities for Research in Astronomy, Incorporated, under NASA contract NAS5-26555.

REFERENCES

Anderson, J., & King, I. R. 2003, PASP, 115, 113
 Bassa, C., et al. 2004, ApJ, 609, 755
 Bassa, C., et al. 2005, ApJ, 619, 1189
 Bedin, L. R., Piotto, G., King, I. R., & Anderson, J. 2003, AJ, 126, 247
 Bellazzini, M., Fusi Pecci, F., Messineo, M., Monaco, L., & Rood, R. T. 2002, AJ, 123, 1509
 Brandt, W. N., et al. 2001, AJ, 122, 2810
 Broos, P. S., Townsley, L. K., Getman, K., & Bauer, F. E. 2002, ACIS Extract, An ACIS Point Source Extraction Package (University Park: Pennsylvania State Univ.)
 Bolte, M. 1992, ApJS, 82, 145
 Clark, G. W. 1975, ApJ, 199, L143
 Cool, A. M., Grindlay, J. E., Cohn, H. N., Lugger, P. M., & Bailyn, C. D. 1998, ApJ, 508, L75
 Davies, M. B. 1997, MNRAS, 288, 117
 Djorgovski, S. 1993, ASP Conf. Ser. 50: Structure and Dynamics of Globular Clusters, 50, 373
 Dolphin, A. E. 2000, PASP, 112, 1383
 Edmonds, P. D., Gilliland, R. L., Heinke, C. O., & Grindlay, J. E. 2003, ApJ, 596, 1177
 Edmonds, P. D., Gilliland, R. L., Heinke, C. O., Grindlay, J. E., & Camilo, F. 2001, ApJ, 557, L57
 Freeman, P. E., Kashyap, V., Rosner, R., & Lamb, D. Q. 2002, ApJS, 138, 185
 Green, P. J., et al. 2004, ApJS, 150, 43
 Grindlay, J. E., Heinke, C., Edmonds, P. D., & Murray, S. S. 2001a, Science, 292, 2290
 Grindlay, J. E., Heinke, C. O., Edmonds, P. D., Murray, S. S., & Cool, A. M. 2001b, ApJ, 563, L53
 Hack, W., & Cox, C. 2001, Instrument Science Report ACS 2001-008 (<http://www.stsci.edu/hst/acs/documents/irs/irsr0108.pdf>)
 Harris, W. 1996, AJ, 112, 1487
 Heinke, C. O., Edmonds, P. D., Grindlay, J. E., Lloyd, D. A., Cohn, H. N., & Lugger, P. M. 2003a, ApJ, 590, 809

Heinke, C. O., Grindlay, J. E., Lugger, P. M., Cohn, H. N., Edmonds, P. D., Lloyd, D. A., & Cool, A. M. 2003b, ApJ, 598, 501

Heinke, C. O., Grindlay, J. E., Edmonds, P. D., Cohn, H. N., Lugger, P. M., Camilo, F., Bogdanov, S., & Freire, P. C. 2005, ApJ, 625, 796

Hertz, P., & Grindlay, J. E. 1983, ApJ, 275, 105

Katz, J. I. 1975, Nature, 253, 698

Peterson, C. J. 1993, ASP Conf. Ser. 50: Structure and Dynamics of Globular Clusters, 50, 337

Pooley, D., et al. 2002a, ApJ, 569, 405

Pooley, D., et al. 2002b, ApJ, 573, 184

Pooley, D., et al. 2003, ApJ, 591, L131

Predehl, P., & Schmitt, J. H. M. M. 1995, A&A, 293, 889

Sarazin, C. L., Irwin, J. A., Rood, R. T., Ferraro, F. R., & Paltrinieri, B. 1999, ApJ, 524, 220

Trager, S. C., Djorgovski, S., & King, I. R. 1993, ASP Conf. Ser. 50: Structure and Dynamics of Globular Clusters, 50, 347

van den Berg, M., Tagliaferri, G., Belloni, T., & Verbunt, F. 2004, A&A, 418, 509

Verbunt, F. 2001, A&A, 368, 137

Verbunt, F. 2002, in ω Cen, a unique window into astrophysics, eds. F. van Leeuwen, Hughes, J. & G. Piotto, ASP Conf. Ser. 265, 289

Verbunt, F. 2003, ASP Conf. Ser. 296: New Horizons in Globular Cluster Astronomy, 296, 245

Verbunt, F., & Lewin, W. H. G. 2004, in Compact Stellar X-ray Sources, astro-ph/0404136

Webbink, R. F. 1985, in Dynamics of Star Clusters, ed. J. Goodman & P. Hut (Dordrecht: Reidel), 541

Zacharias, N., Urban, S. E., Zacharias, M. I., Wycoff, G. L., Hall, D. M., Monet, D. G., & Rafferty, T. J. 2004, AJ, 127, 3043